IISE Transactions

ISSN: (Print) (Online) Journal homepage: www.tandfonline.com/journals/uiie21

Statistical and dynamic model of surface morphology evolution during polishing in additive manufacturing

Adithyaa Karthikeyan, Soham Das, Satish T.S. Bukkapatnam & Ceyhun Eksin

To cite this article: Adithyaa Karthikeyan, Soham Das, Satish T.S. Bukkapatnam & Ceyhun Eksin (2024) Statistical and dynamic model of surface morphology evolution during polishing in additive manufacturing, IISE Transactions, 56:12, 1331-1345, DOI: 10.1080/24725854.2023.2264889

To link to this article: https://doi.org/10.1080/24725854.2023.2264889

View supplementary material

Published online: 29 Nov 2023.

Submit your article to this journal

Article views: 335

View related articles

View Crossmark data

Full Terms & Conditions of access and use can be found at
https://www.tandfonline.com/action/journalInformation?journalCode=uiie21

IISE TRANSACTIONS
2024, VOL. 56, NO. 12, 1331–1345
https://doi.org/10.1080/24725854.2023.2264889

Taylor & Francis
Taylor & Francis Group

Check for updates

Statistical and dynamic model of surface morphology evolution during polishing in additive manufacturing

Adithyaa Karthikeyan, Soham Das, Satish T.S. Bukkapatnam, and Ceyhun Eksin

Department of Industrial and Systems Engineering, Texas A&M University, College Station, TX, USA

ABSTRACT

Many industrial components, especially those realized through 3D printing undergo surface finishing processes, predominantly, in the form of mechanical polishing. The polishing processes for custom components remain manual and iterative. Determination of the polishing endpoints, i.e., when to stop the process to achieve a desired surface finish, remains a major obstacle to process automation and in the cost-effective custom/3D printing process chains. With the motivation to automate the polishing process of 3D printed materials to a desired level of surface smoothness, we propose a dynamic model of surface morphology evolution of 3D printed materials during a polishing process. The dynamic model can account for both material removal and redistribution during the polishing process. In addition, the model accounts for increased material flow due to heat generated during the polishing process. We also provide an initial random surface model that matches the initial surface statistics. We propose an optimization problem for model parameter estimation based on empirical data using KL-divergence and surface roughness as two metrics of the objective. We validate the proposed model using data from polishing of a 3D printed sample. The procedures developed makes the model applicable to other 3D printed materials and polishing processes. We obtain a network formation model as a representation of the surface evolution from the heights and radii of asperities. We use the network connectivity (Fiedler number) as a metric for surface smoothness that can be used to determine whether a desired level of smoothness is reached or not.

ARTICLE HISTORY
Received 21 December 2022
Accepted 28 August 2023

KEYWORDS
Additive manufacturing; polishing; surface morphology evolution; network formation; dynamic models; material removal and material redistribution

1. Introduction

The North American metal polishing market registered a market value of around USD 13.2 billion in 2019. It is poised to witness unprecedented growth at a compound annual growth rate of about 9% over the forecast period of 2021–2027, due to the rising applications of additive manufacturing in various industry verticals such as healthcare, automotive, aerospace and defense sectors (Anon, 2020). Metal Additive Manufacturing techniques allow for the creation of freeform components out of hard-to-process alloys with unique material properties. The rapid solidification and cooling rates during AM can result in a fine-grained microstructure, leading to improved mechanical properties such as higher strength and enhanced fatigue resistance. Nevertheless, existing Additive Manufacturing (AM) methods are often accompanied by post-processing techniques such as polishing in order to improve surface finish and reduce surface porosity (Franco *et al.*, 2017; Tammas-Williams *et al.*, 2017). Such finishing operations find high utility in industrial applications where surface morphology and aesthetics are of great importance to the end use customers (Iquebal *et al.*, 2017).

Whereas AM parts offer unique advantages in terms of design flexibility and rapid prototyping, their machinability can pose challenges compared with cast or wrought counterparts, primarily due to strength anisotropy, which is associated with directional solidification and columnar grain growth (Ananda-Kumar *et al.*, 2018). In addition, some alloys fabricated via AM tend to have low thermal conductivity, and exhibit shear localization during their processing (Iquebal *et al.*, 2019). The initial surface roughness of AM parts is typically higher due to the layer-by-layer build-up process. They also have a high tendency towards the occurrence of internal defects such as porosity or voids. This means that AM parts may require more extensive polishing to achieve the same level of smoothness as cast/wrought parts (Lass *et al.*, 2020; Shiyas and Ramanujam, 2021). Polishing techniques for AM parts can require specialized approaches such as laser polishing or vibratory polishing in conjunction with manual interventions to achieve the desired results. The choice of tools, abrasives, and processes might need to be adapted considering factors such as the type of AM technology, material properties, complex geometries and surface features.

Though the practice of polishing has been in existence from time immemorial, the exact mechanism behind

CONTACT Ceyhun Eksin eksinc@tamu.edu
Supplemental data for this article can be accessed online at chttps://doi.org/10.1080/24725854.2023.2264889
Copyright © 2023 "IISE"

polishing is still not completely known. Early theories put forth by Hooke and Newton (Newton, 1730), followed by Herschel (Archard, 1985) viewed polishing as a material removal process at a very fine scale resulting in gradual flattening of the surface. Later, Beilby proposed surface flow and material redistribution as the dominant mechanism due to localized melting at the asperity–abrasive contact based on observations from microscopic images (Beilby, 1921). Experiments conducted by Winter and McDonald (1969) and Everaerts *et al.* (2019), showed the development of high-residual compressive stress at the metal surface during polishing, thereby providing indications of plastic flow on the surface. Iquebal *et al.* (2019) presented experimental evidence through Scanning Electron Microscope (SEM) images to show that material removal prevailed only during the initial stages of polishing, and surface smoothening was largely a result of material flow and redistribution. The SEM observations at later stages of polishing revealed viscous flow at the asperity–abrasive sliding contacts, involving material flow towards the asperity sides in the form of thin fluid-like layers—see Figure 1. This lateral flow of material continued until the effective distance between neighboring asperities reduced to a critical value, after which bridging occurred resulting in a uniformly smooth surface. Inspired by these experimental observations, here we propose a lumped mass system model that captures the surface morphology evolution due to material removal and redistribution.

Modeling and simulation of polishing processes pose a unique set of challenges, due to the stochastic nature of the asperity–abrasive interaction compared with other material removal processes such as milling and turning. The decision making involved in polishing process as to when to change the polishing pad and when to stop polishing relies heavily on the practitioner's visual inspection and prior experience. Repeated stoppages and surface inspections consume a significant amount of process time. Jin *et al.* (2019) proposed Gaussian process-based decision rules for determining pad change and endpoint condition for polishing, by detecting change patterns in correlation characteristics of the surface.

Various analytical models published in the literature focus on estimating the polishing pad and surface asperity contact temperature rise for different materials. Jaeger (1942) provided flash temperature estimates at the asperity–abrasive sliding contact by considering two semi-infinite planes of different geometrical configurations with constant heat flux over the instantaneous surface of contact. Bulsara *et al.* (1997) determined the maximum and average temperature rise at the abrasive – workpiece contact in a polishing process assuming the workpiece to be perfectly rigid and nondeformable. Horng *et al.* (2004) proposed an analytical model for temperature rise at asperity–abrasive contact during polishing by combining the micro-contact model and contact temperature model, and studied the effects of particle size, particle density, pad hardness and surface roughness values on temperature. A transient heat transfer model was proposed by Mondal *et al.* (2015) to estimate the flash temperature in a pin-on-disk tribometer in view of the variation in coefficient of friction. Iquebal *et al.* (2019) probed the estimated flash temperature for Ti-6Al-4V as a function of asperity–abrasive contact radii and asperity heights using Carslaw and Jaegar's circular moving heat source model (Carslaw and Jaeger, 1959). The heat partition between the asperity and the abrasive particle was determined based on Blok's postulate (Blok, 1937) by setting equal the maximum (quasi-steady state) temperatures of asperity and abrasive particle within the contact. Several models and simulation studies for estimating material removal rate during polishing have been reported in the literature (Evans *et al.*, 2003; Jeng *et al.*, 2003). However, none of them explain the surface

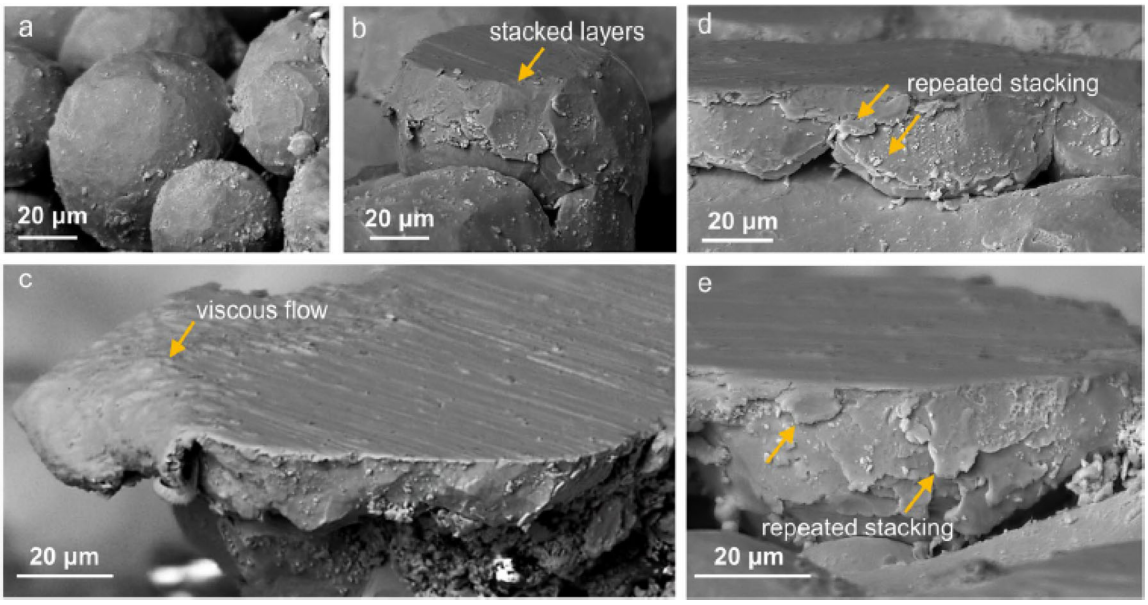

Figure 1. SEM images showing the evolution of spherical asperity structure of 3D printed Ti-6Al-4V samples due to polishing as a result of complex material flow patterns (Iquebal *et al.*, 2019).

plastic flow and material redistribution phenomenon that has been experimentally observed in polishing of metals. Therefore, understanding the exact phenomenology that governs the surface morphology evolution during post-processing stages is essential for developing accurate mathematical models to achieve desired specifications.

The literature provides clear evidence that surface modification during polishing of additive manufactured metals takes place due to material redistribution (Iquebal *et al.,* 2019) as well as material removal (Jeng and Huang, 2005). Currently, there does not exist a single model that captures surface evolution in polishing that combines both material removal and material redistribution phenomena. Here, we provide an analytical lumped mass system model coupled with network formation dynamics to capture the following: (i) the effect of load distribution under various asperity dispersion; (ii) the effect of heat generated during polishing, as well as the resulting material property modification; and finally, (iii) the phenomenon of bridging that is responsible for smoothing of surfaces, due to material redistribution. Specifically, the model represents a surface asperity distribution by a set of spherically curved tops with different heights and diameters. The distribution of the heights and radii determine the load-bearing asperities during the polishing process and the surface roughness. The dynamic model captures the increasing asperity temperatures due to the energy released upon contact. The temperature modulates the material flow versus removal, which determines the rate of decrease in heights and increase in radius of each load-bearing asperity.

The dynamic model requires an initialization of the set of asperities and their properties that best matches the surface roughness of the work piece. We provide a random surface model for determining initial asperity heights and radii that matches the empirical surface characteristics, e.g., density and roughness. We also propose a novel objective for model parameter fitting based on experimental data. The objective considers a weighted combination of difference in surface roughness and Kullback–Leibler (KL) divergence between the model and empirical height distributions. We observe that minimizing a suitably chosen weighted combination of these metrics yields more desirable parameter fits than minimizing solely either of these metrics (difference in surface roughness or KL divergence).

We use the surface measurements from a prior experimental study to fit the model and track the evolution of surfaces for both the model and the experiments. The experiments were conducted in the Smart Manufacturing Lab at the Department of Industrial and Systems Engineering in Texas A&M University on 3D printed Ti-6Al-4V alloy samples. We show that our proposed model is able to capture the time evolution of a surface, and accurately estimate the height distribution of asperities at various polishing stages, with consistent small KL divergence values and minimal difference in surface roughness, when compared to experimental surface measurements. More importantly, this modeling methodology can be generalized to multiple material systems because of the use of lumped mass system approach using the algorithms/procedures provided. Lastly, we map the heights and radii distribution of the surface asperities to a network. This mapping provides a novel network formation model coupled with the lumped mass system dynamics, wherein the network connectivity serves as a metric for tracking surface evolution. The contributions of this article are fourfold:

1. We propose the first lumped mass system model that captures the evolution of the surface during polishing due to material removal and redistribution.
2. The model allows for apportioning the surface modification due to the contribution of material removal vs. redistribution. Specifically, we identify that although material removal is a major factor at the beginning, material redistribution is the major driver of surface smoothing in the later stages of polishing.
3. We propose a novel objective for parameter fitting, that is a weighted combination of KL divergence and difference in surface roughness between the model and experimental height distributions. This weighted objective is able to identify surface characteristics that are in better agreement with empirical data than either of the individual metrics (KL divergence, and difference in surface roughness) considered alone.
4. We propose a novel initial surface model that systematically generates a distribution of asperity heights and radii in accordance with the empirical surface metrics. Together with the parameter fitting procedure, the initialization allows for a mapping of the validated surface model to a network formation model which can then be used as a criterion to determine when to stop polishing.

1.1. *Related literature on modeling surface polishing*

Prior models of surface polishing focus on either material removal or redistribution driven by experimental evidence.

1.1.1. Material removal

The goal is to characterize Material Removal Rate (MRR) as a function of the downward pressure, relative velocity and tool wear via a physical model (Jeng and Huang, 2005; Jackson and Streator, 2006; Guiot *et al.,* 2011; Rao *et al.,* 2013). All of these studies build on a micro-contact model that describe the relation between two surfaces in contact. The essence of these models is that all surfaces are microscopically rough, and the roughness of the surface can be represented by a distribution of asperities represented by spheres (Greenwood and Williamson, 1966), ellipses (Jeng and Wang, 2003) or multi-scale asperities (Majumdar and Bhushan, 1990). Given the contact geometry and asperity distribution, e.g., density and asperity size, the effective force on each asperity is computed so that the total down force is balanced by the sum of the forces acting on each asperity. The balance of forces corresponds to a separation distance between the polishing pad and the surface, which

determines the active surface area on each asperity. Together with the relative velocity, the active surface area corresponds to a MRR that is dependent on the material hardness (density of particles) (Jeng and Huang, 2005). These models are inherently static, i.e., rely on a snapshot of the surface, and do not consider changes in the surface profile as a result of material removal. Moreover, in many cases it is unlikely that material abrasion is the main driver of surface smoothing given that material removal would only expose subsurface pores (Beilby, 1921).

1.1.2. Material redistribution

The premise is that the plastic flow of the surface is the dominant mechanism in the smoothing of the surface during polishing instead of abrasion. Indeed, the formation of a Beilby layer, i.e., plastic flow resulting in filling of pores and bridging asperities, is documented by experimental findings for different materials (Beilby, 1921; Bowden and Hughes, 1937; Sundaram *et al.,* 2012; Iquebal *et al.,* 2019). Some of these works also indicate that the plastic flow of material may be due to high flash temperatures in the range 700–900K reached during polishing (Iquebal *et al.,* 2019). Given the experimental evidence and the inadequacy of the material removal theory, recent efforts focused on modeling material flow and formation of bridges.

A recent modeling approach in this direction represents the surface as a random planar graph with each node (asperity) having a disk shape, i.e., a radius (Bukkapatnam *et al.,* 2018; Iquebal *et al.,* 2019). A link represents a merger or bridging between two asperities. The radius of an asperity grows as the polishing continues. As the disks approach each other, the probability of forming a link grows. While it is noted that the thermomechanical state of the material, as well as the process parameters (down force and velocity), determine the rate of change in radii, these efforts rely on *in situ* images to quantify the change in radii. In contrast, here we provide a physical model of how thermomechanical and micro-contract structures can together affect the changes in asperity geometry.

In doing this, we consider a spherical asperity whose contact with the polishing pad depends on the down force balancing as per the approach of Greenwood and Williamson (1966). The contact at an asperity leads to material removal and material flow dynamics. The material flow at an asperity means a reduction in height and growth in its radius. The speed of change in asperity features (height and radius) depends on the local temperature. The local temperature rises with the down force and the relative velocity. Together these mechanisms and feedbacks constitute a lumped mass dynamical system of material surface morphology during polishing that account for the two experimentally validated major drivers of surface polishing: material removal and flow.

This article is organized as follows. Section 2 describes the principle behind using a lumped mass system approach and the governing differential equations that capture the time evolution of asperity heights, radii and temperature as a result of polishing. Section 3 describes the initial surface model and a procedure for finding the optimized model parameters based on experimental data. Section 4 presents the polishing data that is used in Section 5 for initial surface model generation and parameter fitting. Section 6 provides a mapping of the model state (heights and radii of asperities) to a spatial network. With this mapping, the lumped mass system model is represented as a network formation model where the connectivity of the network represents the surface smoothness. We end with concluding remarks in Section 7.

2. Thermomechanical interactions and surface asperity dynamics during a polishing process

The surface is composed of a distribution of asperities with a specific geometry, here conically shaped with spherically curved tops. Such a realization of asperity geometry at the surface becomes possible as we systematically control the 3D printing process such as Direct Energy Deposition, Electron Beam Melting and Selective Laser Melting (Iquebal *et al.,* 2019). In many AM processes it is not unusual for the surfaces to bear some signatures of the powders, especially when printed under low power settings. These signatures tend to be non-directional and the asperity structure tends to be radially symmetric (Karayel and Bozkurt, 2020). In this model, we represent the surface of a 3D printed workpiece using N asperities, each having a spherical radius R_i at its top, height $h_i(t)$ and temperature $T_i(t)$ at a particular instant of time t where $i \in \{1, 2, 3, ..., N\}$ (Faraon, 2005). The surface radius $r_i(t)$ is initially assumed to be $R_i \times \sin(1^\circ)$ at time $t = 0$ and increases with time as a result of flattening of the asperity top due to polishing.

A polishing process, as depicted in Figure 2(a), applies a total down force $F(t)$ on the workpiece surface via the polishing pad that rotates at speed $s(t)$. The total force acting on the surface is borne by a set of asperities, denoted as "active asperities". The force acting on each asperity F_i is calculated based on Hertz theory (Johnson, 1985) as follows:

$$F_i(t) = \frac{2}{3}\sqrt{r_i(t)}E'\max((h_i(t) - d(t))^{3/2}, 0), \qquad (1)$$

where the constant $E' = \frac{1-\nu_1^2}{E_1} + \frac{1-\nu_2^2}{E_2}$ with E_1 and E_2, and ν_1 and ν_2 are the elastic moduli and Poisson's ratio of the two bodies in contact, respectively. The term $d(t)$ in (1) represents the height of the polishing pad that is obtained by equating the sum of forces acting on each asperity, i.e., $F = \sum_{i=1}^{N} F_i(t)$ where $F_i(t)$ is given in (1) (see Figure 2(b) for a pictorial description). The max operator in (1) means that an asperity is "active", i.e., bears a load, if $d(t) < h_i(t)$. We solve for $d(t)$ at every time t using an iterative process where we increase its value starting from zero until the sum of individual forces equal to the total down force F. The applied load gets distributed to all the active asperities. As polishing continues, i.e., t increases, the heights of active asperities decrease, and new active asperities emerge as they come in contact with the pad.

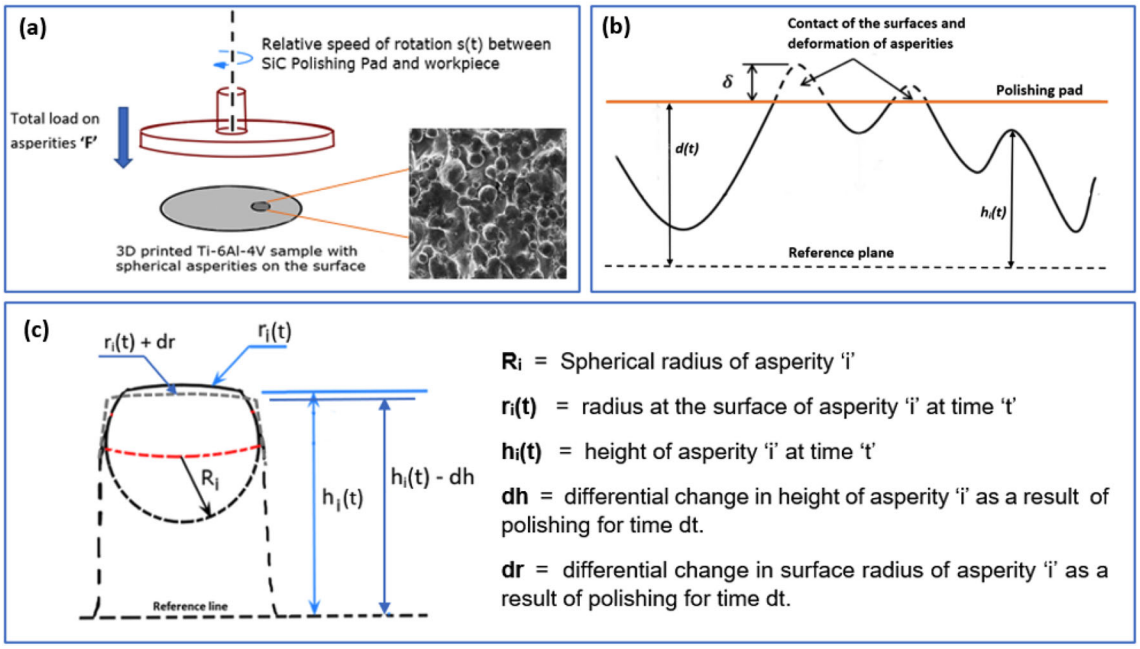

Figure 2. (a) Pictorial representation of the polishing process. (b) Graphic describing the contact between polishing pad and surface asperities during the polishing process. Here $d(t)$ indicates the height of the polishing pad and δ refers to the gap between polishing pad and active asperities used in calculating their load distribution. (c) Geometric representation of an asperity peak with its top getting progressively flattened as a result of polishing.

The down force acting on the asperity $F_i(t)$ and the relative speed between the pad and workpiece $s(t)$ increases the temperature of the asperity T_i,

$$\frac{\partial T_i}{\partial t} = -\alpha(T_i(t) - T_o) + (\kappa_1 F_i(t) + \kappa_2 s(t)), \tag{2}$$

where α is the cooling constant, T_0 is the room temperature (20°C), and κ_1 and κ_2 are heating constants that depend on the abrasive pad and the workpiece. We note that the temperature is determined by repeated flashing at the point of contact between the surface asperity and the polishing pad (Iquebal *et al.*, 2019). The flash temperature at the contact point is significantly higher compared with other regions in the asperity. We consider the temperature T_i in (2) as the "bulk" temperature affected by energy released through repeated flashing. In conventional finishing processes, this temperature increase is generally neglected due to the high thermal conductivity of the material as well as the use of large volumes of coolant and slurry. However, such temperature variations and their influence on the material properties cannot be ignored under ultraprecision manufacturing.

We assume the bulk temperature of an asperity $T_i(t)$ affects the material redistribution at the asperity – polishing pad contact by determining the rate of change in the asperity height $h_i(t)$ as follows,

$$\frac{\partial h_i}{\partial t} = -\sigma_i(t) T_i(t) F_i(t), \tag{3}$$

where

$$\frac{\partial \sigma_i}{\partial t} = \frac{\beta}{T_0}\frac{\partial T_i}{\partial t}, \tag{4}$$

and temperature diffusion constant $\beta \geq 0$. The height of an asperity decreases with down force $F_i(t)$. The rate of decrease in height of active asperities is proportional to its current temperature $T_i(t)$ and heat carrying capacity $\sigma_i(t)$ modeled as a first-order approximation proportional to the total rate of change in the temperature as per (4).

The radii of active asperities at the point of contact increase at a rate proportional to the decrease in height (see Figure 2(c)). In particular, the radius of asperity i, denoted with $r_i(t)$, evolves as follows

$$\frac{\partial r_i}{\partial t} = -\eta_i(t)\rho_i(t)\frac{\partial h_i}{\partial t}. \tag{5}$$

where $\eta_i(t)$ is the fraction of material redistributed, and $\rho_i(t) > 0$ maps the decrease in height of asperity i to an increase in radius of the asperity. Material redistribution rate is always between zero and one, where $\eta_i(t) = 1$ means material is fully conserved whereas $\eta_i(t) = 0$ means material is fully removed during polishing. Empirically, we find that material removal is dominant in the initial stages, i.e., $\eta_i(t)$ is small, and material redistribution tends to dominate in later stages, i.e., $\eta_i(t)$ tends to increase toward one. The mapping $\rho_i(t)$ depends on the spherical shape of the initial asperity and the ratio between height and radius. In particular, the larger is the height compared to the radius, the faster is the growth in radius per unit of height reduction. In Section 5.2, we provide a functional form for $\eta_i(t)$ and $\rho_i(t)$ based on experimental data obtained from polishing 3D printed Ti-6Al-4V samples.

2.1. Remarks on the surface asperity dynamics

When the down force $F = 0$ is zero and polishing speed $s(t) = 0$ (i.e., there is no spin), solving for polishing pad height in (1) and $F = \sum_{i=1}^{N} F_i(t)$ yields that $d(t) = \max_{i=1,\ldots,N} h_i(t)$. Thus, the heights and radii of surface

asperities ($h_i(t)$ and $r_i(t)$) remain invariant with time even when $T_i(t) > T_0$ if $F = 0$.

The dynamics begin to develop when the down force F and material redistribution fraction $\eta_i(t)$ are positive (> 0) for $i = 1, \ldots, N$. To see this, note that there is at least one load-bearing asperity with $F_i(t) > 0$ when $F > 0$. This is because $d(t) < h_i(t)$ holds true for at least one asperity $i = 1, \ldots, N$ irrespective of the radii and height values. For a load-bearing asperity i, the temperature will always be above the room temperature, i.e., $T_i(t) > T_0$. Accordingly, the force acting on the asperity will reduce the asperity height and increase its radius for a positive fraction of material redistribution $\eta_i(t) > 0$ as per (3) and (5), respectively.

Under a constant down force F, once a spherical asperity becomes active, its radius begins to increase at a rate proportional to the rate of decrease of its height as per (5). This results in the pad height (displacement) to equate acting and bearing forces at higher values. As a result, the total down force gets distributed to all active asperities in a manner proportional to the square root of the radii at their points of contact and also ensures the pad height to continuously decrease along with the decrease in heights of active asperities, as indicated in Figure 3. We note that the initial asperity structure and the dominant mechanism in polishing can differ for different materials fabricated via different 3D printing methodologies. However, the lumped mass system framework and the governing differential equations can be altered accordingly to capture the variations in the initial asperity structure and track the surface morphology evolution for different polishing speeds and down force.

The model makes a few simplifying assumptions regarding the polishing process. Note that the pad's relative speed affects the temperature as per (2). However, a positive down force will continue to change the surface asperity configuration, even if the relative speed of the pad is zero. This is not quite realistic, and thus we assume that the polishing pad always has a positive relative speed. This means our model ignores the effects of the pad's relative speed on the changes in the radii and heights through the redistribution rate. The prior works on polishing showed that the polishing speed affects the pad–workpiece tribology, including the asperity wear mechanism and friction (Luo and Dornfeld, 2001). However, significant effects on MRRs were observed only with very high polishing speeds (> 1000 rpm) as in the case of magnetic float polishing (Jiang *et al.*, 1998). Other approaches discussed the effect of polishing speed on the thermal aspects of the process (Komanduri and Hou (2000, 2001a, 2001b)). Similarly, we assume, per (4) that the material softens linearly with temperature. This may hold true when the temperature values are far from the glass transition temperature of the material (Beilby, 1921; Iquebal *et al.*, 2019).

3. Initial surface model and parameter fitting

3.1. Initial surface model

The model described in the previous section expects a set of N asperities with initial heights ($h_i(0)$), radii ($r_i(0)$), and temperature values $T_i(0)$. We assume all asperities are at room temperature initially. We determine the number of asperities, and initial height of each asperity using statistics and material properties available in practice. In particular, we rely on (i) surface packing density, (ii) surface roughness of the material, and (iii) surface measurements obtained from optical profilers. We generate empirical distributions of heights by using surface data obtained via, e.g., white light interferometry (see Section 4 for details). Given empirical data and material characteristics, we implement the following steps to initialize our model.

A. *Number of asperities and initial radii:* We determine the number of asperities N and radii values ($r_i(t)$) via a random circle packing algorithm that aims to match the desired surface packing density. A surface packing density is given by the ratio of circles to that of the area of a square grid. We consider a random circle packing algorithm by Semechko (2018) that takes in the minimum and maximum allowable radii of circles as input, and employs rejection sampling technique to randomly populate the interior of the

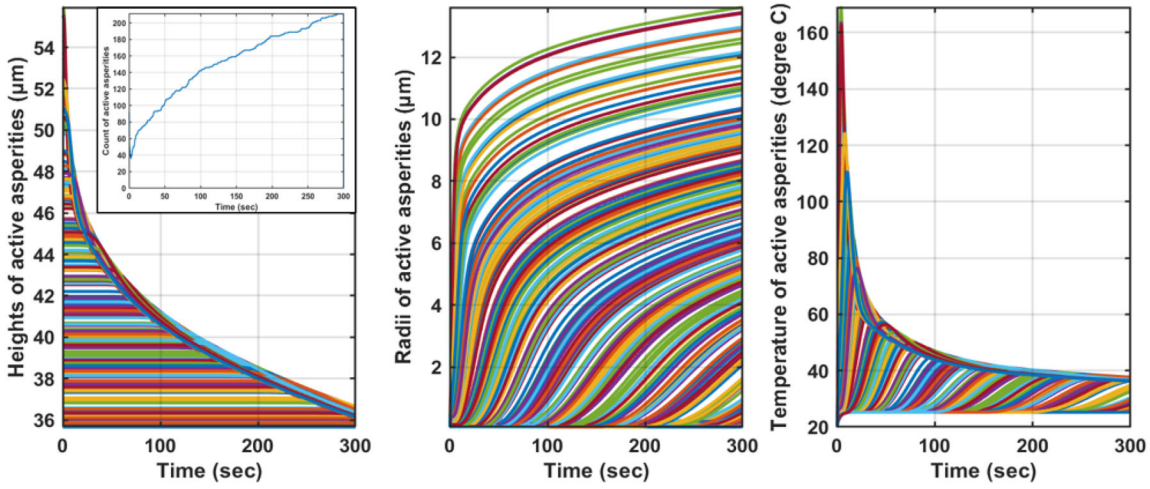

Figure 3. Model dynamics indicating the heights, radii and temperature change of active asperities during the first 5 minutes of polishing. The number of active asperities coming in contact with the pad increases with time during the polishing process (inner panel). The model parameters used in this case are as follows: $[\alpha, \beta, \sigma_0] = [0.3046, 2.42 \times 10^{-4}, 1.82 \times 10^{-3}]$ (Refer Section 5.2 for model parameter fitting).

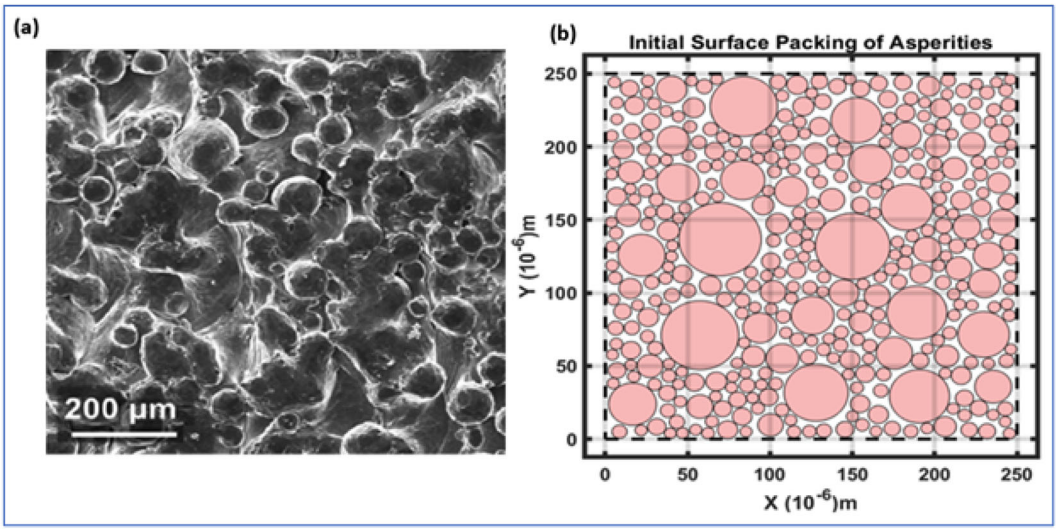

Figure 4. (a) SEM image showing the surface asperities of Ti-6Al-4V metal sample (Reproduced from Iquebal *et al.* (2019)). (b) Spatial distribution of N asperities in a 0.25 mm x 0.25 mm grid with surface packing density of 0.70 generated using a random circle packing algorithm.

grid with non-overlapping circles into a given 2D surface area with radii belonging to the given range. We determine the range of radii, i.e., minimum and maximum values, so that the desired surface packing density can be achieved. The algorithm yields the number of asperities (N) and their associated radii (see Figure 4(b) for an instance of the algorithm, and Procedure A in Algorithm 1, developed based on SEM observations as depicted in Figure 4(a)).

B. *Initial heights:* We determine N height values based on empirical height distributions measured using white light interferometry. In particular, we fit a distribution to empirical height distribution, and sample N height values according to the fitted height distribution (see Procedure B in Algorithm 1).

C. *Mapping heights to asperities:* In the last step, we associate the realized N height values with N asperities so that the surface characteristics match the average surface roughness value. We measure the surface roughness by estimating the standard deviation or the **Sa**[1] value of heights of asperities. Estimating the standard deviation of heights empirically involves collecting height measurements from random locations on the workpiece. This implies that the height values are not drawn uniformly at random, but rather proportional to the radii of the asperity. In the initialization of our model, we implement a mapping procedure to assign each height value to an asperity (with a given radii) so that the initial surface is true to the estimated surface roughness (procedure C in Algorithm 1). The mapping procedure begins with arbitrarily assigning the N height values to N asperities. For each assignment, we obtain multiple height samples from each asperity proportional to its radii considering the curvature of the asperity, i.e., sampled points further away from the center have smaller height values than the height at the center node – see Algorithm 1 in Supplementary Materials for details. The histograms of the sampled heights and data are compared using the Kolmogorov–Smirnov (KS) Test. We shuffle the height values assigned to each asperity until we get a significant p-value from the KS Test and the surface roughness is close to the empirical data.

Algorithm 1 *Initial surface generation*

procedure A. Determine the number of asperities and their radii
  Input: Surface dimensions $d_1 \times d_2$, surface packing density $0 < \rho < 1$ and
    Maximum and minimum allowable circle radius $\phi_{\max} > \phi_{\min} > 0$.
  Implement random circle packing algorithm.
  Output: $N \in \mathbb{N}$ and $R = \{R_i\}_{i=1}^{N}$
end procedure
procedure B. Generate asperity heights
  Input: Empirical height values $\tilde{h}$. (obtained from metal sample before polishing)
    Fit a distribution μ_h to $\tilde{h}$
    Draw N height values from μ_h
  Output: $h = \{h_i(0)\}_{i=1}^{N}$
end procedure
procedure C. Map heights to asperities
  Input: Heights $h(0) \in \mathbb{R}^{N\times 1}$, sphere radii $\{R_i\}_{i=1}^{N}$, surface radii $r(0) \in \mathbb{R}^{N\times 1}$,
    minimum sampling size k, approximation level L, threshold p-value $\bar{p}$,
    and threshold **Sa** value difference $\bar{v}$
  while $p > \bar{p}$ OR $||\mathbf{Sa}_{model} - \mathbf{Sa}_{data}|| > \bar{v}$ **do**
    See the Algorithm in Supplementary Materials for details.
  end while
  Output: $\{(r_i(0), h_i(0))\}_{i=1}^{N}$
  end procedure

3.2. Parameter fitting

We have a system of parameterized differential equations (1)-(5) which govern the evolution of the surface features in response to the polishing process. The evolution of the

[1]Standard deviation is the average squared difference of heights from the mean. **Sa** value is the average absolute difference of heights from the mean.

surface heights, radii, and temperature depends on the values of the model parameters. The model parameters, denoted using $\boldsymbol{\xi}$, include the cooling constant (α), temporal diffusion constant (β), initial value for $\sigma_i(0)$ (σ_0), and any parameter that may come from the functional forms of $\rho_i(t)$ and $\eta_i(t)$ in (5). We formulate an optimization problem to tune the model's parameters so that the height and radii dynamics accurately follow the changes in empirical height distribution of asperities and surface characteristics at different stages of polishing.

At each stage of model fitting, we assume that we have the height distribution of the asperities on the workpiece, denoted using P, and the surface roughness Sa defined as

$$\mathbf{Sa}(h) := \frac{1}{N}\sum_{i=1}^{N} |h_i - \bar{h}| \tag{6}$$

given the empirical height vector $h \in \mathbb{R}^N$ of surface asperities, and $\bar{h} = \frac{1}{N}\sum_{i=1}^{N} h_i$ is the arithmetic mean of the height values.

For the objective function of the optimization problem, we use a weighted combination of the symmetrized KL divergence and the difference between **Sa** values of the simulated and experimental height distributions. Formally, for two probability distributions P and Q defined on the same state space $\mathcal{X}$, the KL divergence is defined as

$$D_{KL}(P||Q) := \sum_{x\in\mathcal{X}} P(x)\log_2\left[\frac{P(x)}{Q(x)}\right] \tag{7}$$

We know that $D_{KL}(P||Q) \geq 0$ and $D_{KL}(P||Q) = 0$ if and only if $P = Q$. In our work we consider the symmetrized KL-divergence which is defined as

$$D(P||Q) := \frac{1}{2}\left(D_{KL}(P||Q) + D_{KL}(Q||P)\right) \tag{8}$$

In symmetrized KL-divergence we have an additional term $D_{KL}(Q||P)$. If P is the empirical height distribution of the surface asperities at a particular stage obtained experimentally, and Q is the height distribution obtained computationally by running the dynamics, then we can interpret $D_{KL}(P||Q)$ as the expected excess surprise from using the distribution Q as a model when the actual distribution is P. Adding the extra term $D_{KL}(Q||P)$ to our objective helps to serve as a role reversal between the distributions obtained. That is, we emphasize the surface information obtained via solution of the model dynamics and experimental observations equally as valid representations of reality.

We compute the difference in **Sa** values between two height distributions P and Q, denoted as $\Delta\mathbf{Sa}(P,Q)$, by computing the Sa values for heights sampled from each distribution and then computing their differences, i.e.,

$$\Delta\mathbf{Sa}(P,Q) := |\mathbf{Sa}(h) - \mathbf{Sa}(\tilde{h})|. \tag{9}$$

where h and $\tilde{h}$ are respectively empirical and model height vectors sampled from P and Q.

Given the two metrics ($D(P||Q)$ and $\Delta\mathbf{Sa}(P,Q)$) defined above, we have the following optimization problem for parameter fitting

$$\begin{aligned} &\min_{\xi}\ \lambda D(P||Q) + (1-\lambda)\Delta\mathbf{Sa}(P,Q) \\ &s.t.\ \ Q = \zeta_{\bar{t}}(x_0;\boldsymbol{\xi}) \end{aligned} \tag{10}$$

where $\lambda \in [0,1]$ is the weight constant, P is the given (empirical) height distribution, $\zeta_t(\cdot)$ is the model dynamics in (1)-(5) that takes an initial height, radii and temperature values $x_0 := \{h_i(0), r_i(0), T_i(0), \sigma_i(0)\}_{i\in N}$, model parameters $\boldsymbol{\xi}$ and time horizon $\bar{t}$ as inputs, and outputs a height distribution Q at time $\bar{t} > 0$. The weight λ gauges the relative importance of the KL divergence term versus the difference in empirical and model's **Sa** values. Figure 5 shows the resulting BACs as λ varies for a given empirical distribution. As λ increases from zero to one, the KL divergence value decreases, but $\Delta\mathbf{Sa}$ increases. The figure also shows that when the difference in surface roughness is the only metric used as a part of the objective function, i.e., when $\lambda = 0$, it leads to an overestimation of surface planarization due to polishing. As λ is increased the Bearing Area Curve (BAC) curve obtained from the model more closely matches the empirical BAC curve, but suffers from a higher mismatch of surface roughness.

Remark: Let $\mathcal{P}(\mathcal{X})$ be the set of all probability distributions defined on the state space $\mathcal{X}$. For a reference distribution P_0, we can consider a subset $C \subset \mathcal{P}(\mathcal{X})$ which does not contain P_0. A solution $Q_0 = \text{argmin}_{Q\in C} D_{KL}(Q||P_0)$ can be interpreted as the orthogonal projection of P_0 onto C. When C is additionally known to be convex, the minimizer Q_0 is unique, and $D_{KL}(Q_0||P_0)$ measures the distance between P_0 and the set C (Lesne, 2014). KL-divergence is often preferred as a distance measure between distributions.

4. Experiments and data

We consider polishing data from a prior experimental study conducted on a 3D printed Ti-6Al-4V sample (Jin *et al.*, 2019). The sample was polished for a total of 16.5 hours approximately by a Buehler Metaserv Grinder-Polisher (model 95-C2348-160) using 800-grit polishing pads made of silicon carbide (SiC). The head and base speeds of the polisher were kept at 100 and 50 rpm, respectively. The down force applied on the workpiece during the polishing process was kept constant at 10 lbs. The polishing process is split into multiple stages where *ZeGage*^{TM} 3D optical profiler, a.k.a "Zygo", was used to collect surface measurements from 32 different locations on the workpiece after each polishing stage. We condensed 3D data to a reduced form by sampling height values from the associated BACs at every location for all stages. The locations on the BAC from which samples were drawn were determined based on a hypothesis test.

In this article, we will consider the first hour of polishing, equivalently six stages, to tune our model parameters and to compare the results of our model. The stages have different polishing time intervals, where each stage lasts 5, 10 and 15 minutes in the first two stages (Stages 1-2), in Stages 3-5, and in Stage 6, respectively. We note that the experimental height measurements of the sample at all stages of polishing were captured using a top-bottom setting in "Zygo" where

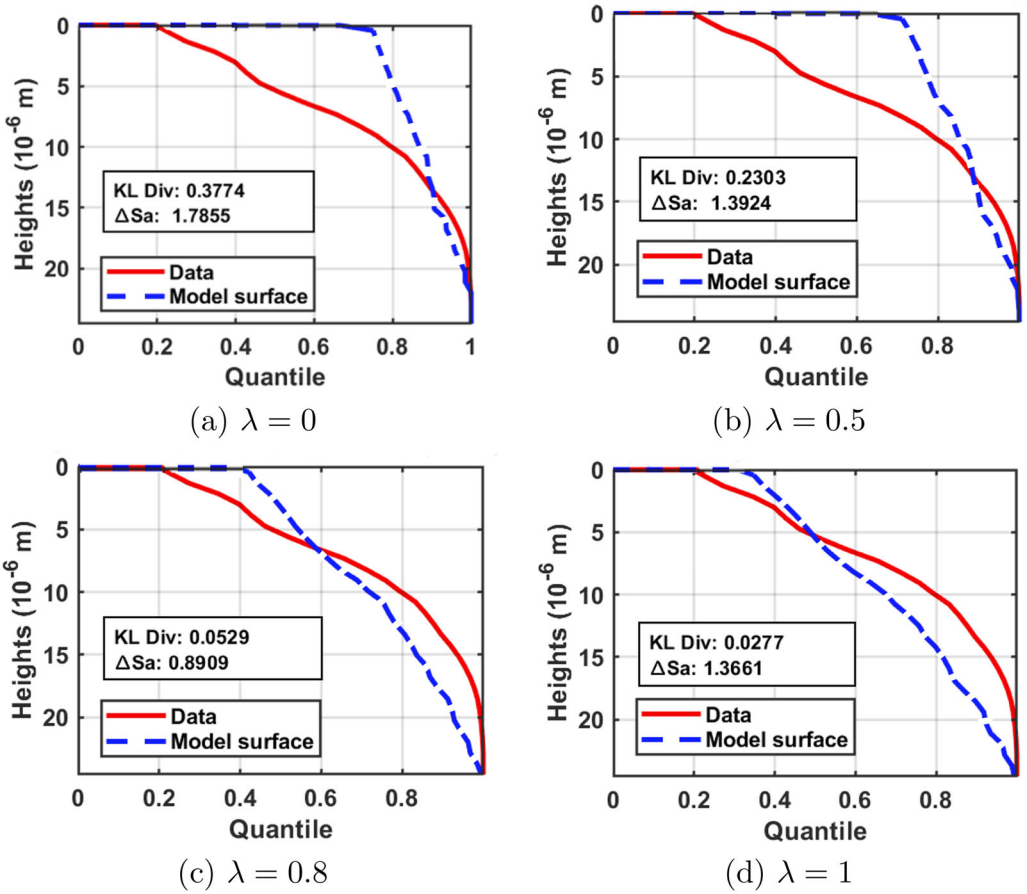

Figure 5. Comparison of the BACs obtained from simulated height distributions after the initial 5 minutes (Stage 1) using optimal parameter values obtained using $\lambda \in \{0, 0.5, 0.8, 1\}$ weights on the KL divergence term in the objective function (10). BAC is a cumulative distribution function plotted against the quantile values. For each λ, we obtain the optimal parameters $[\alpha, \beta, \sigma_0]$ by solving (10) using simulated annealing—see the Appendix for details. The dashed lines and solid line corresponds to BACs for the empirical asperity height distributions and that of actual surface at the end of the first stage of polishing.

the zero line (reference) was set at the top most point of the surface. We subtract our model height values from the maximum height to obtain positive height values. We compare height values between the empirical and model-generated distributions based on these positive values. Here, we use the Stage 0 surface data to initialize the state of the nonlinear dynamics (1)-(5) as per the initial surface generation steps in Section 3, and use the remaining six stages to identify best model parameters.

5. Results

5.1. Initial surface realization

For Ti-6Al-4V metal alloys, we consider a desired surface packing density (ratio of circles to the total area) of 0.7 ($\rho = 0.7$). Such a close packed representation of surface asperities is essential to better understand the elastic–plastic contact mechanism between the surfaces; the polishing pad and the workpiece. We respectively choose the minimum and maximum allowable radii as $\phi_{\min} = 3.65$ μm and $\phi_{\max} = 25.05$ μm so that the random circle packing algorithm can realize the desired packing density given the grid size of $250\mu\text{m} \times 250\mu\text{m}$. One such realized model surface has a total number of $N = 374$ asperities.

The empirical asperity heights is fitted with a Weibull distribution μ_h as shown in Figure 6(a) (Iquebal *et al.*, 2019). We then draw height values for all N asperities in our model from this fitted Weibull distribution corresponding to the height histogram. In the last step, we implement the mapping algorithm using a p-value threshold of $\bar{p} = 0.05$ for the KS test and surface roughness gap threshold chosen as $\bar{v} = 1$ μm. We employ a minimum sampling size of $k = 2$ points for the smallest asperity and an approximation level of $L = 3$ in calculating the heights for the additionally sampled points (refer to Procedure C in Algorithm 1). The height distributions of the realized model surface is shown in Figure 6(b). The BAC for this realized surface is compared with the actual stage 0 data, as depicted in Figure 6(c). Figure 6(d) shows the Q-Q plot between Stage 0 experimental data and the simulated model surface. The KL divergence or the relative entropy between the distributions is also low estimated at 0.0073. The empirical surface roughness values, measured using standard deviation and **Sa**, are close to the ones obtained from the mapping process. In particular, the measured standard deviation and **Sa** values of the metal sample before polishing are 9.8 and 7.9 μm while that of the initial generated model surface are 10.6 and 8.6 μm, respectively.

5.2. Model parameters

After we generate our initial model surface that accurately reflects the characteristics of Stage 0 experimental data, our objective is to capture the dynamics that bring about

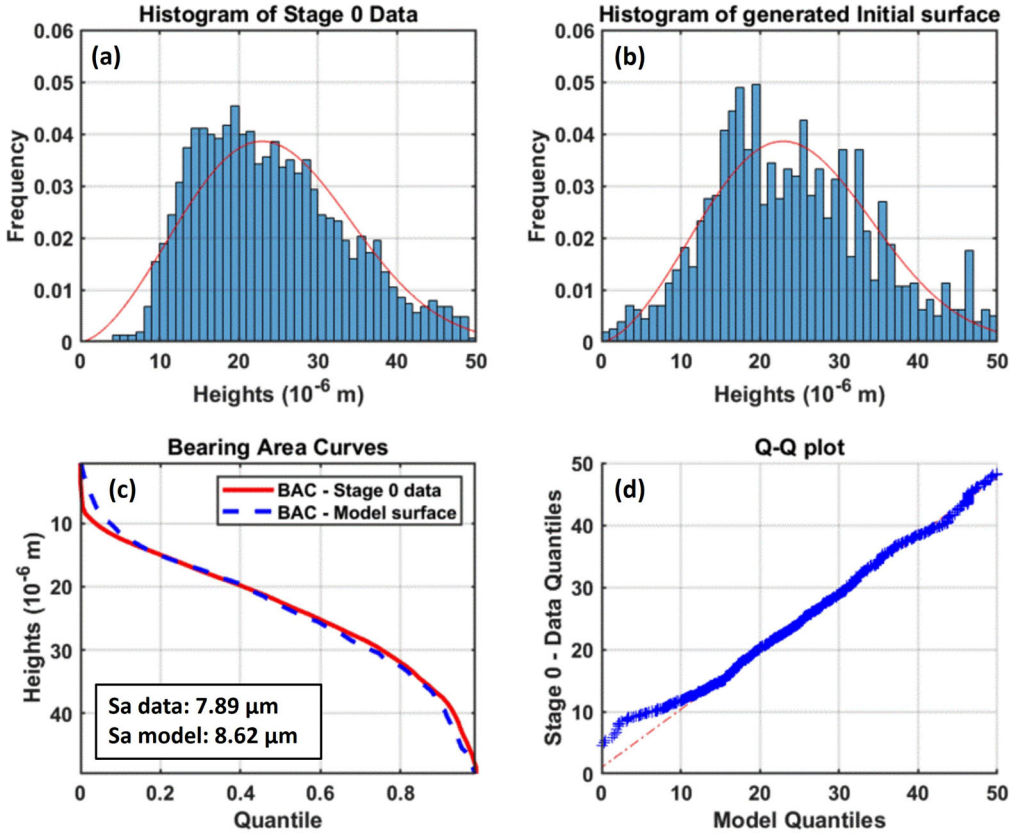

Figure 6. (a) and (b): Comparison between the distribution of asperity heights of the metal sample before polishing and that of model-generated surface using the random circle packing and asperity height mapping algorithm. The corresponding p-value from the two sample KS Test is 0.058. (c) and (d): Comparison of BACs and Q-Q plots between Stage 0 experimental data and simulated model surface.

changes in height distribution of asperities and surface characteristics at different stages of polishing. We begin by determining the functional forms of the height to radius mapping rate $\rho_i(t)$ and the redistribution rate $\eta_i(t)$ defined in (5),

$$\rho_i(t) = \frac{h_i(t)}{4r_i(t)}, \text{ and } \eta_i(t) = \exp\left[-\left(\left(\frac{h_i(t)}{A_0}\right)^{\psi_1} + \left(\frac{A_1}{r_i(t)}\right)^{\psi_2}\right)\right]. \tag{11}$$

The formulation of coefficient ρ_i in (11) captures the differential radii change at the surface of asperities based on the geometry of the spherical curvature at the asperity top by conserving the material volume during each time step of polishing. The formulation of the redistribution rate $\eta_i(t)$ captures the transition from initial significant material removal to increased material redistribution later during polishing.

In simulation of the model dynamics, we observed that constant A_0 values in the order of magnitude 10^2, A_1 and ψ_1 in the order of 10^1 and ψ_2 in the order of $10^{0.1}$ yield comparable and desirable trajectories for the height distribution. The specific values used in this simulation study are $A_0 = 60$, $A_1 = 2.5$, $\psi_1 = 2$ and $\psi_2 = 0.0833$. We also set the heating constants $\kappa_1 = 15$ and $\kappa_2 = 3$. Our exploratory numerical experiments showed that the effects of varying these constants on the dynamics can be captured by modifying the cooling constant α.

Next we solve the model-fitting problem in (10) for the cooling constant (α), temporal diffusion constant (β) and initial value for σ_i (σ_0) parameters, i.e., $\boldsymbol{\xi} = (\alpha, \beta, \sigma_0)$ given the empirical height distributions and surface statistics at each polishing stage. As discussed in Section 3.2, Figure 5 pits the simulated height distributions for Stage 1 against the empirical surface characteristics at Stage 1 using optimal parameter values $[\alpha, \beta, \sigma_0]$ obtained via different weights on the KL divergence term ($\lambda \in \{0, 0.5, 0.8, 1\}$) in the objective function (10). As per Figure 5, small values of the weight constant λ tend to overestimate the extent of surface planarization due to polishing. Given this observation, we fix the weight constant in the objective of (10) to $\lambda = 0.8$ for all the stages.

To compute the objective at a particular stage k, we take the asperity heights h_k obtained computationally and pass it through a post-processing operation where we sample additional points at every asperity i proportional to its radii R_i^2 as in step 3 of Algorithm 1. This allows us to have an expanded height vector $\tilde{h}_k$ that accounts for more accurate geometric information of the actual surface profile thereby increasing the accuracy of our calculations. We obtain the empirical height distribution $\tilde{P}$ from the height samples obtained experimentally at stage k.

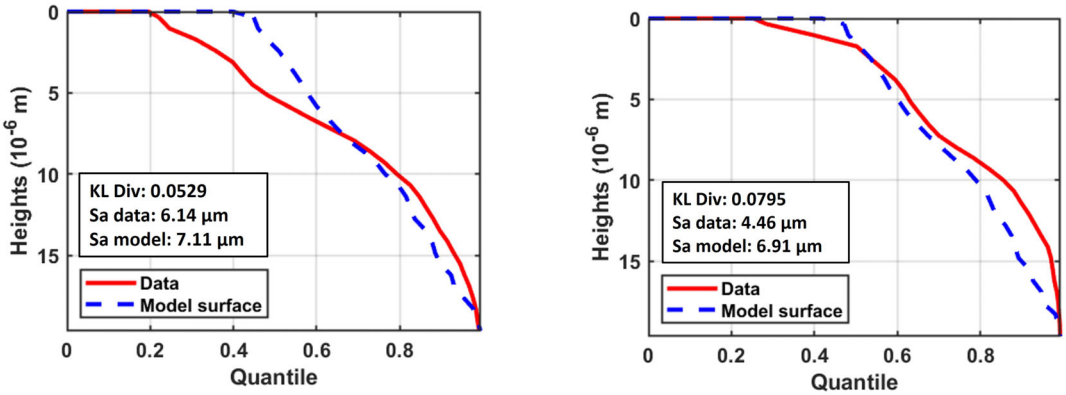

(a) $[\alpha, \beta, \sigma_0] = [0.3046, 2.42 \times 10^{-4}, 1.82 \times 10^{-3}]$ (b) $[\alpha, \beta, \sigma_0] = [0.1086, 0.29 \times 10^{-4}, 0.1 \times 10^{-3}]$

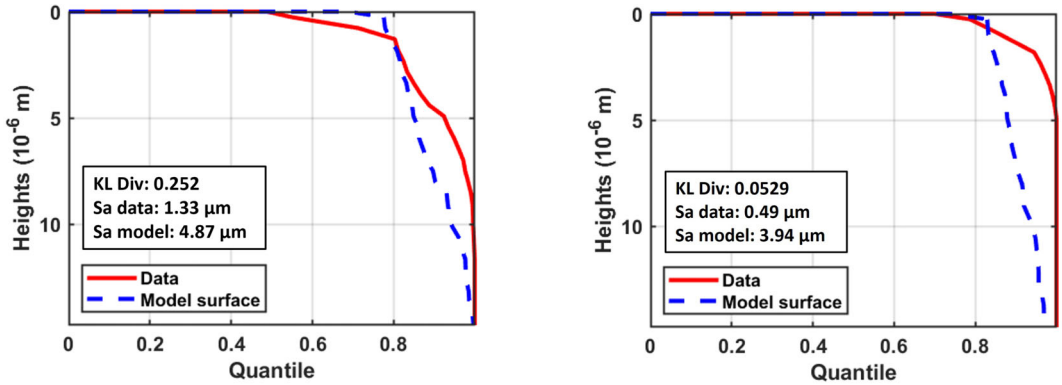

(c) $[\alpha, \beta, \sigma_0] = [1.3722, 2.33 \times 10^{-4}, 3.5 \times 10^{-3}]$ (d) $[\alpha, \beta, \sigma_0] = [2.013, 0.38 \times 10^{-4}, 2.7 \times 10^{-3}]$

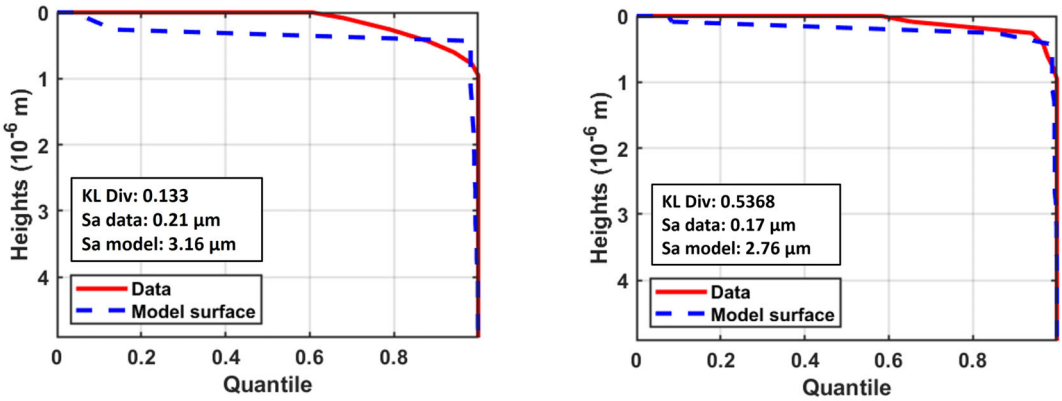

(e) $[\alpha, \beta, \sigma_0] = [1.3434, 19 \times 10^{-4}, 4.5 \times 10^{-3}]$ (f) $[\alpha, \beta, \sigma_0] = [1.6508, 14 \times 10^{-4}, 7.9 \times 10^{-3}]$

Figure 7. Comparison of BACs between actual surface and modeled surface computed using values for the parameters α, β, and σ_0 for Stages 1-6 respectively (ordered top to bottom, left to right) of the polishing process assuming the weight on the entropy term is $\lambda = 0.8$ in (10).

Figure 7 shows the optimal values for α, β and σ_0, and the corresponding BACs for the six stages (Stages 1-6). We observe that the height distributions and surface roughness values obtained from the model closely match those obtained from the data validating that the model can replicate the surface morphology evolution for an hour of polishing (Stages 1-6). The **ΔSa** values varies between 0.89 and 3.53, and KL-divergence values range between 0.05 and 0.53 over the stages. Initially, the model slightly overestimates the extent of surface planarization—see Stage 1. In later stages, we find the model surface to slightly underestimate the level of planarization—see Stage 5.

6. Network formation dynamics

An important goal for modeling surface polishing dynamics is to be able to automatically determine when to stop polishing based on surface smoothness (Bukkapatnam *et al.*, 2018). To do this, we propose a method for tracking the surface smoothness based on a network representation of the surface characteristics obtained from the validated model.

We consider the set of asperities as the set of nodes in the network and use Delaunay triangulation to determine the neighborhood structure of each asperity. Accordingly,

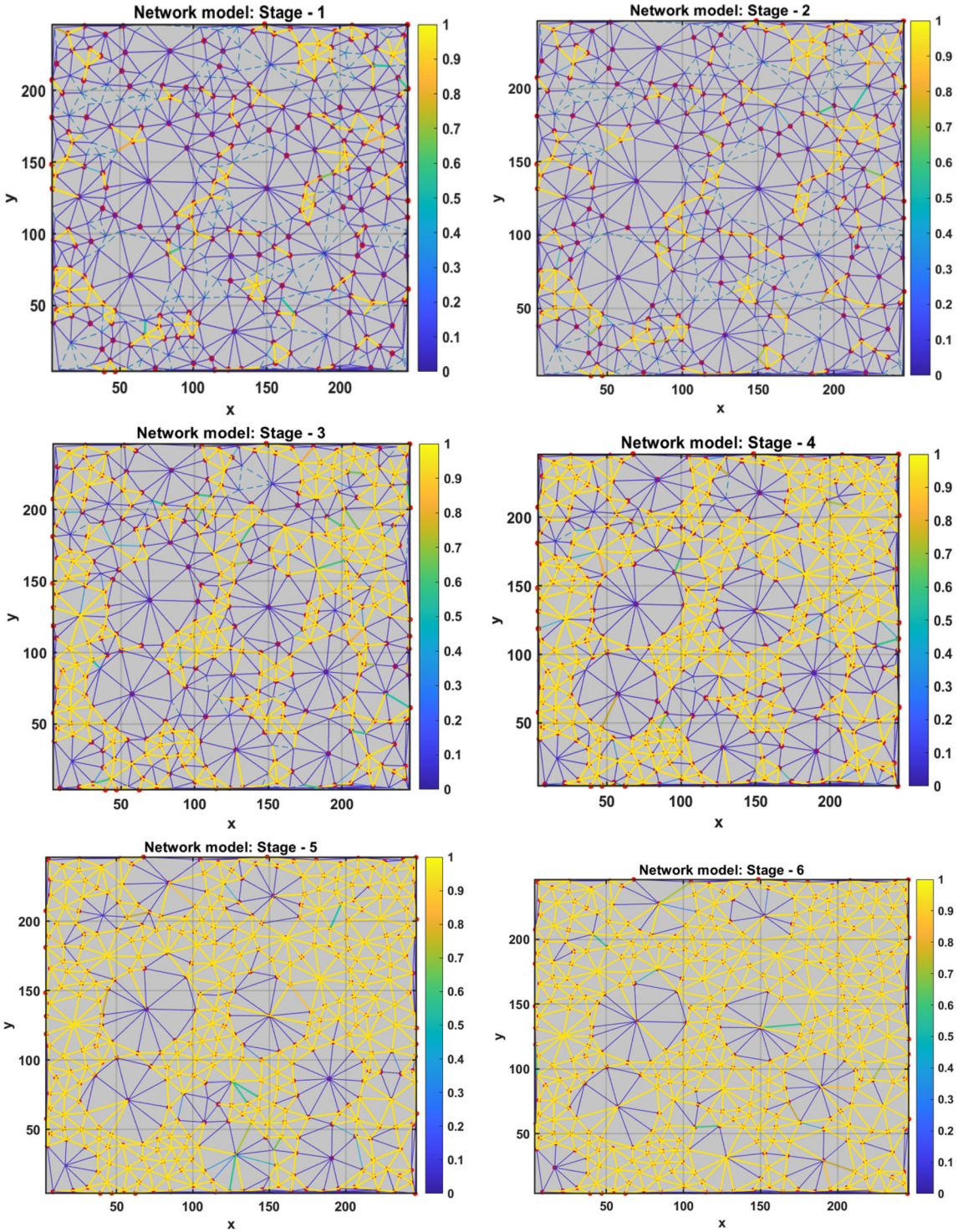

Figure 8. Network evolution with stages as a result of material redistribution due to polishing.

asperities that are part of the same triangle are potential neighbors. The existence of an edge between asperity i and its neighbor j depends on whether the two asperities form a bridge as depicted in Figure 1(f-g). As in Bukkapatnam *et al.* (2018), we consider a probabilistic model of edge (bridge) formation between nodes i and j. The probability of existence of edge $i-j$ (e_{ij}) depends on distance between asperities d_{ij} and their radii $r_i(t)$ and $r_j(t)$,

$$e_{ij}(t) \propto \frac{\xi_{ij}(t)^{n-1} e^{-\xi_{ij}(t)/2}}{(n-1)!} \tag{12}$$

where $\xi_{ij}(t) := 2\pi\rho\,(d_{ij} - (r_i(t) + r_j(t)))^2$, n is the number of nodes in the graph, and recall that ρ is the surface packing density. According to (12), the edge probability $e_{ij}(t)$ increases as $\xi_{ij}(t)$ decreases over time with increasing asperity radii.

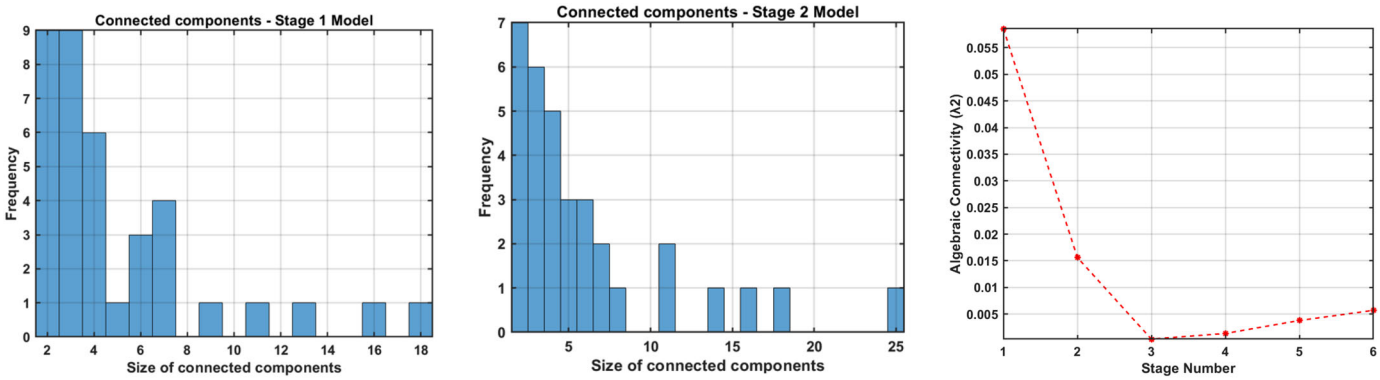

Figure 9. Network evolution. (a-b) Distribution of connected components for stages 1 and 2. From stage 3 onwards, the network has only one large connected component with 373 nodes.(c) Fiedler number of the largest connected component in each stage.

We construct an evolving network by considering the edge probabilities in (12) for each pair of potential neighboring asperities. We note that while the network representation of the surface is due to Bukkapatnam *et al.* (2018), the model dynamics in (1)-(11) drive the changes in the radii $r_i(t)$. In contrast, Bukkapatnam *et al.* (2018) estimates the asperity radii from images taken after every stage. Figure 8 shows the realized network after each stage where the edge probabilities are color coded and x and y axes in μ m. When we assume there is an edge between nodes i and j if $e_{ij}(t) > \bar{e}$ where $\bar{e} = 0.85$ is a chosen threshold, we find the size of the largest connected component to grow from 18 in Stage 1 to 330 in Stage 3. At the end of Stage 6, all but one of the asperities ($N - 1 = 373$) are connected based on the threshold $\bar{e}$. We show the distribution of connected components for Stages 1 and 2 in Figure 9(a-b). As expected, the number of disconnected nodes decreases, and the size of the largest connected component increases. We consider the second largest eigenvalue of the largest connected component (Fiedler number) as a measure for the smoothness of the surface per Rao *et al.* (2015) and Bukkapatnam *et al.* (2018). Figure 9(c) shows that the Fiedler number begins to increase after Stage 3 when the largest connected component reaches a size comparable to the number of nodes in the network, $N = 374$. The network connectivity measured by the distribution of the connected components and Fiedler number of the largest connected component parameterized by the threshold $\bar{e}$ can serve as a guide in determining the smoothness of the surface and when to terminate the polishing process.

7. Conclusions and discussion

In this article, we developed a dynamic model of surface morphology evolution of 3D printed materials during a polishing process. The dynamic model can account for both material removal and redistribution during the polishing process. In addition, the model accounts for increased material flow due to heat generated during the polishing process. We provide a set of procedures for model initialization and parameter estimation based on empirical data. We used these procedures to validate the proposed model on a 3D printed Ti-6Al-4V sample polished by a Buehler Metaserv Grinder-Polisher (model 95-C2348-160) using polishing pads made of silicon carbide (SiC). The model fitting confirms prior results that material removal is limited to early stages of polishing. The procedures developed make the model applicable for other 3D printed materials and polishing processes.

A major motivation for the model is to automate the polishing process of 3D printed components. An important goal in automating the polishing process is to determine whether or not the workpiece has reached the desired smoothness level. Graphical representations of the spatio-temporal evolution of surface morphology have been effective in enabling endpoint detection and prediction capabilities in the finishing of additively manufactured components (Bukkapatnam *et al.*, 2018). We obtain a network formation model as a representation of the surface evolution from the distribution of asperity heights and radii where the active asperities in contact with the polishing pad act as nodes and the likelihood of asperities to merge is indicated by edge weights connecting the nodes. We propose a novel method using Delaunay triangulation to model the surface connectivity evolution as a result of surface plastic flow at different stages of polishing. We consider the distribution of connected components and network connectivity (Fiedler number) as metrics for surface smoothness that can be used to determine whether a desired level of smoothness is reached or not.

Funding

The authors acknowledge the generous support from United States National Science Foundation (NSF) under **ECCS-1953694**.

Notes on contributors

Adithyaa Karthikeyan is currently a PhD student specializing in advanced manufacturing within the Department of Industrial and Systems Engineering, Texas A&M University, USA. He received his B.Tech (Hons) degree in mechanical engineering from the National Institute of Technology, Tiruchirappalli, India in 2017 and MS degree in interdisciplinary engineering from Texas A&M University in 2020. He was a summer intern with Micron Technology Inc. in 2023 with their CMP (Chemical Mechanical Planarization) process development

team for semiconductor manufacturing. His research interests include mathematical modelling and data analytics for manufacturing processes and systems.

Soham Das is a PhD student in the Department of Industrial and Systems Engineering at Texas A&M University, USA. He received his B.Tech degree in mechanical engineering from NIT Durgapur, India in 2017. His research lies at the intersection of game theory and combinatorial optimization, such as in the control of learning in network games.

Satish T.S. Bukkapatnam is the Rockwell International Professor of Industrial and Systems Engineering at Texas A&M University, and the Director of Texas A&M Engineering Experiment Station Institute of Manufacturing Systems. He received his PhD degree in industrial and manufacturing engineering from Pennsylvania State University (1997). His research interests are broadly in smart manufacturing systems, and ultraprecision manufacturing. Dr. Bukkapatnam is a Fellow of IISE and SME, Associate Member of CIRP, and was a Fulbright-Tocqueville Distinguished Chair.

Ceyhun Eksin received his BS degree in control engineering from Istanbul Technical University, Istanbul, Turkey, in 2005, an MS degree in industrial engineering from Boğaziçi University, Istanbul, Turkey in 2008, an MA degree in statistics from Wharton Statistics Department, University of Pennsylvania, Philadelphia, PA, 19103, USA in 2015, and a PhD degree in electrical and systems engineering from the Department of Electrical & Systems Engineering, University of Pennsylvania, Philadelphia, PA, USA in 2015. He was a postdoctoral researcher jointly affiliated with Schools of Biological Sciences, and Electrical and Computer Engineering, Georgia Institute of Technology, Atlanta, GA, USA. He is currently an assistant professor in the Department of of Industrial and Systems Engineering at Texas A&M University, College Station, TX, USA. He is a recipient of NSF CAREER award in 2023. His research interests are in the areas of networks, game theory, control theory, and distributed optimization. His current research focuses on game theoretic learning and decentralized optimization with applications to autonomous teams, epidemics, and energy systems.

ORCID

Adithyaa Karthikeyan http://orcid.org/0000-0002-5886-7251
Soham Das http://orcid.org/0000-0001-7655-3697
Satish T.S. Bukkapatnam http://orcid.org/0000-0003-3312-8222
Ceyhun Eksin http://orcid.org/0000-0001-9329-9301

References

Ananda-Kumar, R.K., Moscoso-Kingsley, W., Jacob, G., Donmez, A. and Madhavan, V. (2018) Machining behavior of additively manufactured and cast-wrought nickel-based superalloy (in 625). *Procedia Manufacturing*, **26**, 595–606.

Anon (2020) *North America Metal Polishing Market Outlook 2027*, Research Nester Pvt. Ltd. https://www.researchnester.com/reports/north-america-metal-polishing-market/2829

Archard, J.F. (1985) Mechanical polishing of metals: A scientific argument of long standing. *Physics Bulletin*, **36**, 212–214.

Beilby, G.T. (1921) *Aggregation and Flow of Solids: Being the Records of an Experimental Study of the Micro-structure and Physical Properties of Solids in Various States of Aggregation*, 1900–1921. Macmillan and Company, Limited, London, UK.

Blok, H. (1937) In *Proceedings of the General Discussion on Lubrication and Lubricants*. IMech E, London, pp. 222–235.

Bowden, F.P. and Hughes, T. (1937) Physical properties of surfaces iv—polishing, surface flow and the formation of the Beilby layer. *Proceedings of the Royal Society of London. Series A-Mathematical and Physical Sciences*, **160**(903), 575–587.

Bukkapatnam, S.T., Iquebal, A.S. and Kumara, S.R. (2018) Planar random graph representations of spatiotemporal surface morphology: Application to finishing of 3-d printed components. *CIRP Annals*, **67**(1), 495–498.

Bulsara, V.H., Ahn, Y., Chandrasekar, S. and Farris, T.N. (1997) Polishing and lapping temperatures. *Journal of Tribology*, **119**(1), 163–170.

Burke, E.K. and Kendall, G. (2014) *Search Methodologies: Introductory Tutorials in Optimization and Decision Support Techniques*. Springer.

Carslaw, H.S. and Jaeger, J.C. (1959) *Conduction of Heat in Solids*. Clarendon Press, Oxford.

Evans, C., Paul, E., Dornfeld, D., Lucca, D., Byrne, G., Tricard, M., Klocke, F., Dambon, O. and Mullany, B. (2003) Material removal mechanisms in lapping and polishing. *CIRP Annals*, **52**(2), 611–633.

Everaerts, J., Salvati, E. and Korsunsky, A.M. (2019) Nanoscale depth profiling of residual stresses due to fine surface finishing. *Advanced Materials Interfaces*, **6**(21), 1900947.

Faraon, I. (2005) Mixed lubricated line contacts. PhD Thesis, University of Twente Twente, The Netherlands.

Franco, B.E., Ma, J., Loveall, B., Tapia, G.A., Karayagiz, K., Liu, J., Elwany, A., Arróyave, R. and Karaman, I. (2017) A sensory material approach for reducing variability in additively manufactured metal parts. *Scientific Reports*, **7**(1), 3604.

Greenwood, J. and Williamson, J. (1966) Contact of nominally flat surfaces. *Proceedings of the Royal Society of London (A)*, **295**, 300–319.

Guiot, A., Pattofatto, S., Tournier, C. and Mathieu, L. (2011) Modeling of a polishing tool to simulate material removal. *Advanced Materials Research*, **223**, 754–763.

Horng, J.H., Jeng, Y.R. and Chen, C.L. (2004) A model for temperature rise of polishing process considering effects of polishing pad and abrasive. *Journal of Tribology*, **126**(3), 422–429.

Iquebal, A.S., El Amri, S., Shrestha, S., Wang, Z., Manogharan, G.P. and Bukkapatnam, S. (2017) Longitudinal milling and fine abrasive finishing operations to improve surface integrity of metal AM components. *Procedia Manufacturing*, **10**, 990–996.

Iquebal, A.S., Sagapuram, D. and Bukkapatnam, S.T.S. (2019) Surface plastic flow in polishing of rough surfaces. *Scientific Reports*, **9**(21).

Jackson, R.L. and Streator, J.L. (2006) A multi-scale model for contact between rough surfaces. *Wear*, **261**(11–12), 1337–1347.

Jaeger, J.C. (1942) Moving sources of heat and the temperature at sliding contacts. *Journal and Proceedings of the Royal Society of New South Wales*, **76**(3), 203–224.

Jeng, Y.-R. and Huang, P.-Y. (2005) A material removal rate model considering interfacial micro-contact wear behavior for chemical mechanical polishing. *Journal of Tribology*, **127**(1), 190–197.

Jeng, Y.R., Huang, P.Y. and Tsai, H.J. (2007) Theoretical investigation for the material removal rate of metal polishing process, in *Proceedings of the 35th International MATADOR Conference: Formerly The International Machine Tool Design and Research Conference*, Springer, London, pp. 207–210.

Jeng, Y.-R. and Wang, P.-Y. (2003) An elliptical microcontact model considering elastic, elastoplastic, and plastic deformation. *Journal of Tribology*, **125**(2), 232–240.

Jiang, M., Wood, N.O. and Komanduri, R. (1998) On chemo-mechanical polishing (cmp) of silicon nitride (si3n4) workmaterial with various abrasives. *Wear*, **220**(1), 59–71.

Jin, S., Iquebal, A., Bukkapatnam, S., Gaynor, A. and Ding, Y. (2019) A Gaussian process model-guided surface polishing process in additive manufacturing. *Journal of Manufacturing Science and Engineering*, **142**, 1–17.

Johnson, K. (1985) *Contact Mechanics*. Cambridge University Press, Cambridge, UK.

Karayel, E. and Bozkurt, Y. (2020) Additive manufacturing method and different welding applications. *Journal of Materials Research and Technology*, **9**(5), 11424–11438.

Komanduri, R. and Hou, Z. (2000) Thermal modeling of the metal cutting process: Part i—Temperature rise distribution due to shear plane heat source. *International Journal of Mechanical Sciences*, **42**(9), 1715–1752.

Komanduri, R. and Hou, Z. (2001a) A review of the experimental techniques for the measurement of heat and temperatures generated in

some manufacturing processes and tribology. *Tribology International*, **34**(10), 653–682.
Komanduri, R. and Hou, Z.B. (2001b) Thermal modeling of the metal cutting process—part iii: Temperature rise distribution due to the combined effects of shear plane heat source and the tool–chip interface frictional heat source. *International Journal of Mechanical Sciences*, **43**(1), 89–107.
Lass, E.A., Zhang, F. and Campbell, C.E. (2020) Nitrogen effects in additively manufactured martensitic stainless steels: Conventional thermal processing and comparison with wrought. *Metallurgical and Materials Transactions A*, **51**, 2318–2332.
Lesne, A. (2014) Shannon entropy: A rigorous notion at the crossroads between probability, information theory, dynamical systems and statistical physics. *Mathematical Structures in Computer Science*, **24**(3), e240311.
Luo, J. and Dornfeld, D.A. (2001) Material removal mechanism in chemical mechanical polishing: Theory and modeling. *IEEE Transactions on Semiconductor Manufacturing*, **14**(2), 112–133.
Majumdar, A. and Bhushan, B. (1990) Role of fractal geometry in roughness characterization and contact mechanics of surfaces. *Journal of Tribology*, (2), 205–216.
Mondal, M.K., Biswas, K. and Maity, J. (2016) A transient heat transfer model for assessment of flash temperature during dry sliding wear in a pin-on-disk tribometer. *Metallurgical and Materials Transactions A*, **47**, 600–607.
Newton, I. (1730) *Opticks: Or, a Treatise of the Reflections, Refractions, Inflections and Colours of Light*. Dover Publications, New York, 1979.
Rao, P.K., Beyca, O.F., Kong, Z., Bukkapatnam, S.T., Case, K.E. and Komanduri, R. (2015) A graph-theoretic approach for quantification of surface morphology variation and its application to chemical mechanical planarization process. *IIE Transactions*, **47**(10), 1088–1111.
Rao, P.K., Bhushan, M.B., Bukkapatnam, S.T., Kong, Z., Byalal, S., Beyca, O.F., Fields, A. and Komanduri, R. (2013) Process-machine interaction (pmi) modeling and monitoring of chemical mechanical planarization (cmp) process using wireless vibration sensors. *IEEE Transactions on Semiconductor Manufacturing*, **27**(1), 1–15.
Semechko, A. (2018) Random circle packing algorithm using rejection sampling - MATLAB CODE (https://www.mathworks.com/matlabcentral/answers/405186-fill-area-with-random-circles-having-different-diameters#answer_324684), MATLAB Central Answers.
Shiyas, K. and Ramanujam, R. (2021) A review on post processing techniques of additively manufactured metal parts for improving the material properties. *Materials Today: Proceedings*, **46**, 1429–1436.
Sundaram, N.K., Guo, Y. and Chandrasekar, S. (2012) Mesoscale folding, instability, and disruption of laminar flow in metal surfaces. *Physical Review Letters*, **109**(10), 106001.
Tammas-Williams, S., Withers, P.J., Todd, I. and Prangnell, P.B. (2017) The influence of porosity on fatigue crack initiation in additively manufactured titanium components. *Scientific Reports*, **7**(1), 7308.
Winter, P.M. and McDonald, W.J. (1969) Biaxial residual surface stresses from grinding and finish machining 304 stainless steel determined by a new dissection technique. *Journal of Basic Engineering*, **91**(1), 15–22.

Appendix

A simulated annealing algorithm for parameter estimation

We utilize an instance of the simulated annealing algorithm (Burke and Kendall, 2014) to obtain a solution to (10). Let the vector ξ consist of an assignment for the values of the parameters $\xi = [\alpha, \beta, \sigma_0]$. Let $f(\xi)$ represent the objective value for the chosen parameters ξ in (10). We run the dynamics $\zeta_{\bar{t}}(x_0; \xi)$ for the duration of the stage $\bar{t}$ in order to compute the objective function value in (10).

Algorithm 2 *Simulated Annealing Algorithm*

1: **Initialize** ξ_{start}, C_0, L_0
2: $k \leftarrow 0$
3: $\xi \leftarrow \xi_{start}$
4: **while** stopcriterion is *FALSE* **do**
5: **for** $l = 1, \ldots L$ **do**
6: **Generate** ξ' from $\mathcal{N}(\xi)$
7: **if** $f(\xi') \leq f(\xi)$ **then**
8: $\xi \leftarrow \xi'$
9: **else**
10: **if** $\exp\left[(f(\xi) - f(\xi'))/C_k\right] > U[0,1)$ **then**
11: $\xi \leftarrow \xi'$
12: **end if**
13: **end if**
14: **end for**
15: $k \leftarrow k + 1$
16: **Update** C_k
17: **end while**

The simulated algorithm (Algorithm 2) begins with an initial solution $\xi_{start} \in \Omega$, where Ω represents the set of all possible values for the parameters. Here, we consider a warm-start where we draw 10,000 random points from Ω, and pick the one that obtains the minimum objective value. We define a neighborhood of a solution $\xi \in \Omega$ as $\mathcal{N}(\xi)$, where $\mathcal{N}(\cdot) : \Omega \rightarrow 2^{\Omega}$, is a hyper-rectangular space around ξ. In contrast to *iterative improvement* procedures where in each step we move to a solution in the neighborhood with a better objective value, here we allow for controlled violations, i.e., accept, in a limited way, solutions that have worse objective values. The control parameter C_k for every stage k manages the probability of accepting solutions of poorer quality (Step 10). We update the values for these control parameters using the function (Step 16). For our implementation, we consider the geometric update rule where the value of C_k is lowered at every stage using $C_{k+1} = \delta C_k, \delta \in (0,1)$. Initially at large values of C_k, large deteriorations are accepted. As C_k decreases, only smaller deteriorations are accepted, and finally as the value of $C_k \rightarrow 0$, solutions that obtain better objective value are accepted. For the stopping criterion, we set the algorithm to stop when the value of the optimal objective does not change by an order of magnitude of 10^{-6} over a series of iterations.

Since $P = \zeta_{\bar{t}}(x_0; \xi)$ is the solution of a set of coupled nonlinear ordinary differential equations, the objective function is non-convex and has potentially multiple local solutions. Here we do not make analytical claims on the quality of the solution. Instead, we judge the effectiveness of the solution based on whether the dynamics attain a height distribution and Sa values that qualitatively match those given by the experimental data (see Figures 5, 6 and 7).